**Synthesis, Characterization and Thermal Study of Divalent Germanium, Tin and Lead Triazenides for Atomic Layer Deposition**

Rouzbeh Samii,[a] David Zanders,[b],[c] Anton Fransson,[a] Goran Bačić,[b] Sean T. Barry,[b] Lars Ojamäe,[a] Vadim Kessler,[d] Henrik Pedersen,[a] and Nathan J. O'Brien*,[a]

[a] Department of Physics, Chemistry and Biology, Linköping University, SE-581 83 Linköping, Sweden

[b] Department of Chemistry, Carleton University, 1125 Colonel By Drive, Ottawa, Ontario, K1S5B6, Canada

[c] Faculty of Chemistry and Biochemistry, Ruhr University Bochum, Universitätsstraße 150, 44801, Bochum, Germany

[d] Department of Molecular Sciences, Swedish University of Agricultural Sciences, P.O. Box 7015, 75007 Uppsala, Sweden

*Corresponding author: nathan.o.brien@liu.se

## Abstract

The number of M–N bonded divalent group 14 precursors suitable for atomic layer deposition is limited, in particular for Ge and Pb. A majority of the reported precursors are dicoordinated, with the only tetracoordinated example being the Sn(II) amidinate. No such Ge(II) and Pb(II) compounds have been demonstrated. Herein, we present tetracoordinated Ge(II), Sn(II) and Pb(II) complexes bearing two sets of the bidentate 1,3-di-*tert*-butyl triazenide ligands. These compounds are highly volatile and show ideal behavior by thermogravimetric analysis. However, they have unusual thermal properties and exhibit instability during sublimation. Interestingly, the instability is not only temperature dependent but also facilitated by reduced pressure. Using quantum-chemical density functional theory, a gas-phase decomposition pathway was mapped out. The pathway account for the unusual thermal behavior of the compounds and is supported by electron impact mass spectrometry data.

## Introduction

Group 14 metal chalcogenides are of interest due to their outstanding electrical and optical properties.[1] In particular, the mono-chalcogenides, such as germanium sulfide (GeS)[2], germanium selenide (GeSe)[2], tin sulfide (SnS)[2–9], tin selenide (SnSe)[2,10–12] and lead sulfide (PbS)[13–19] have potential application in future optoelectronic and solar cell technologies. The manufacture of these electronic devices requires the deposition of high-quality thin films with

high control and reproducibility. The films must be conformal, dense, and have low levels of defects and impurities. High-quality thin films are commonly grown by chemical vapor deposition (CVD) methods. One such method is atomic layer deposition (ALD), which is a low temperature alternative CVD, that relies exclusively on surface reactions between precursor molecules and the growing film. To obtain high-quality ALD films, it is of the utmost importance to have metal and non-metal precursors that possess favorable physical and chemical properites.[20] Furthermore, to avoid the need for redox chemistry to occur during deposition, it is preferred to use precursors of the same oxidation state as the material being deposited. An ALD precursor must be thermally stable such that it does not decompose before reaching the film surface for deposition.[21] It should then undergo chemical reactions at the surface to form a stable monolayer and easily removable by-products.[22,23] The chemisorbed surface species should then react with the second precursor (eg. $H_2S$, $H_2O$) in a second self-limited reaction. An ALD precursor must be sufficiently volatile for transport in the gas phase to the reaction chamber. Also, to maximize film growth, the precursor should employ low-steric bulk ligands for effective surface saturation and dense coverage.
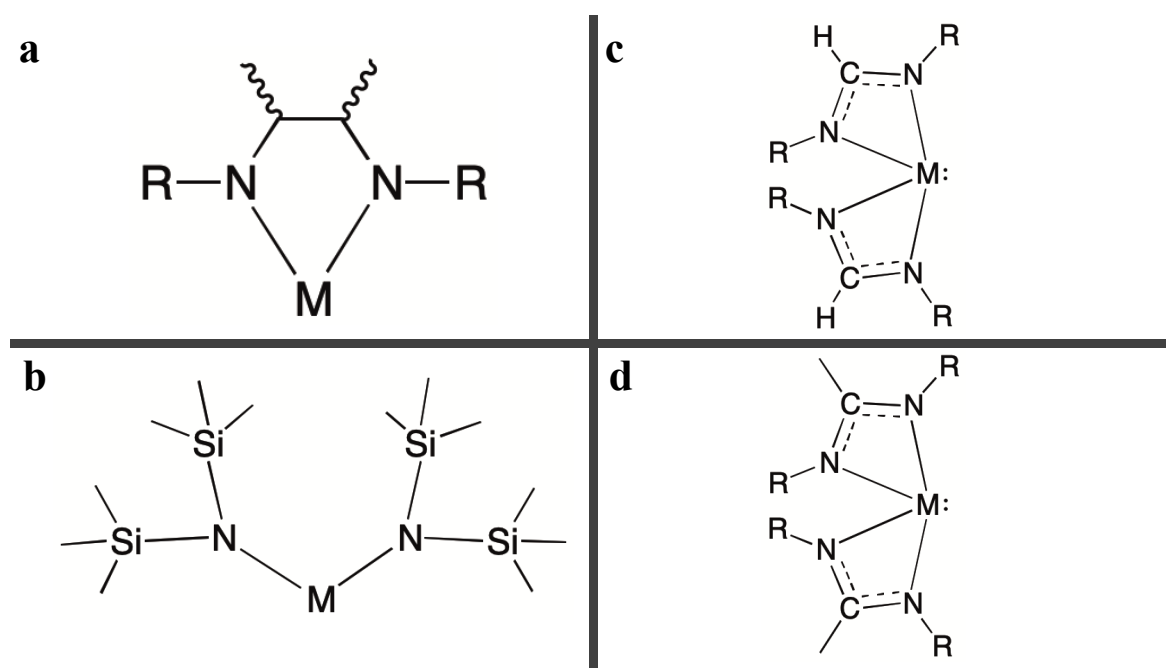


*Figure 1: General structures of divalent cyclic diamide (a), hexamethyldisilazide (b), formamidinate (c) and amidinate (d) metal complexes. These compounds represent the M–N bonded compounds that have been utilized as precursors for group 14 chalcogenides. formamidinate and amidinate (c and d) have only been used for Sn.*

Precursors with M–N bonds are desirable for ALD due to the high reactivity of the polarized bond. To date, there is only a small library of exclusively M–N bonded divalent group 14 metal precursors suitable for ALD. Figure 1 shows the structures of some precursors used for growing

group 14 mono-chalcogenides that are discussed below. The dicoordinated Ge(II) cyclic diamide[24] and hexamethyldisilazides[25] have been used to deposit GeS[24] and GeSe[26] by ALD. However, the deposited GeS was X-ray amorphous whilst the GeSe films contained carbon impurities. SnS have been demonstrated by ALD using the dicoordinated cyclic diamide[24] and tetracoordinated Sn(II) formamidinate and amidinate.[27,28] The amidinate ligand system provides a tetracoordinated, thermally stable and volatile precursors that afford high-quality SnS films with low levels of impurities. More recently, the first example of ALD grown PbS[29] using Pb–N bonded dicoordinated hexamethyldisilazide[25,30] and cyclic diamide[31] precursors. The deposited PbS films were near stoichiometric and had low levels of carbon impurities. Deposition temperature for ALD growth was, however, limited to $\leq 155$ °C due to poor thermal stability of the deposited surface species. To our knowledge, no tetracoordinated and exclusively M–N bonded Ge(II) or Pb(II) precursors suitable for ALD have yet been demonstrated as the Ge(II) and Pb(II) amidinates lack volatility.[32,33] A ligand system closely related to the amidinates are the triazenides, where the endocyclic carbon is replaced a nitrogen.

Although tetracoordinated Ge(II), Sn(II) and Pb(II) triazenides have been reported[34], these bear the 1,3-diphenyltriazenide ligand and are therefore not volatile due to intermolecular π-π interactions in the solid-state. Recently, we explored the 1,3-dialkyltriazenide ligand for group 13 metals and used the 1,3-diisopropyltriazenide In(III) and Ga(III) precursors for ALD of InN and GaN.[35–37] These precursors undergo gas-phase decomposition at higher temperatures to give a smaller and more reactive M(III) species, resulting in improved growth rates film quality. To further investigate the reactivity and thermal properties of the 1,3-dialkyltriazenide ligand, we envisaged its ability to stabilize divalent group 14 elements. This would give a new class of tetracoordinated M–N bonded precursors for ALD. Herein, we present synthesis, characterization and thermal studies of divalent Ge, Sn, and Pb complexes bearing two sets of the 1,3-di-*tert*-butyltriazenide ligand. Their high volatility and unique thermal properties make the group 14 triazenides interesting for use as ALD precursors.

## Results and discussion
### Synthesis and Characterization of Triazenides 1–3.
Reaction of lithium 1,3-di-*tert*-butyltriazenide ligand with MCl$_2$, where M = Ge, Sn or Pb, gave **1**–**3** in good yields after recrystallization (Scheme 1). Compounds **1**–**3** are air- and moisture-sensitive, low melting yellow solids. Compounds **1**–**3** were characterized by nuclear magnetic

resonance (NMR) spectroscopy, X-ray crystallography, mass spectrometry, elemental analysis and melting point measurement.
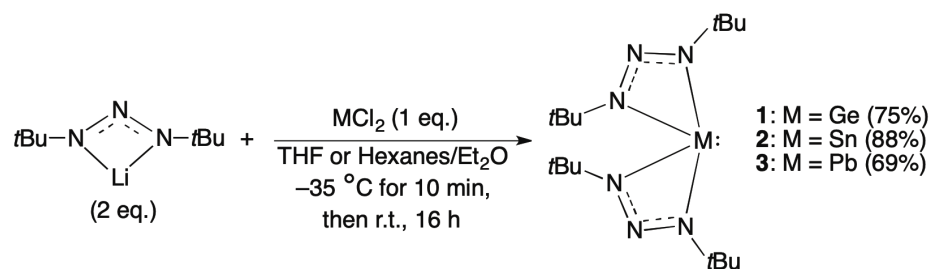


*Scheme 1: General procedure for making **1**–**3**. Synthesis of **1** was carried out in THF while synthesis of **2** and **3** were carried out in a 1:4 mixture of Et$_2$O and n-hexane.*

The $^{1}$H NMR spectra of compounds **1**–**3** showed a singlet between 1.30–1.40 ppm, indicating a fast exchange for all protons of the *tert*-butyl groups. The $^{13}$C NMR spectra of **1**–**3** gave the primary and quaternary carbon peaks between 30.5–30.6 and 58.9–61.1 ppm, respectively. All NMR spectra are presented in the supporting information.

The crystal structure of **1** showed two chelating 1,3-di-*tert*-butyltriazenide ligands on the metal center (Figure 2). Both ligands are forced to the same side of the metal center by a stereochemically active lone pair, situated on the opposite side (Figure 2b). The coordination of the Ge atom is best described as a distorted seesaw geometry, suggested by a geometry index ($\tau_4'$) of 0.65.[38] The crystal structures of compounds **2** and **3** are presented in the supporting information. Compounds **2** and **3** have analogous crystal structures and molecular geometries analogous to **1**, although more distorted towards tetrahedral geometry ($\tau_4'$ = 0.82 and 0.86 for **2** and **3**, respectively). The α-angle decreases in the order **1** > **2** > **3**. This trend can be explained by a greater s-character of the lone pair when moving down the group, from Ge to Pb (Table 2).[39] Having greater s-character, the lone pair will occupy more of the coordination sphere on the metal center, forcing the axial nitrogen atoms closer together which, in turn, give a more acute α-angle.

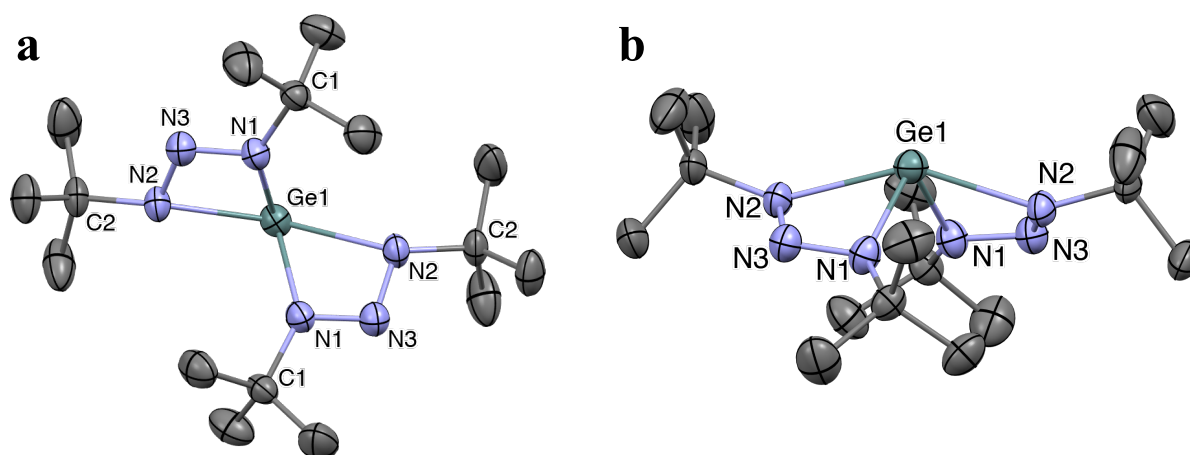Geometries of compounds **1–3** are in good agreement with previously reported analogs, **1A–3A**,[34] employing the bulkier 2,6-diisopropylphenyl (dipp) R-groups in place of *tert*-butyl (Table 1 and 2).

*Table 1. Average bond lengths in Å for **1–3** (R = tert-butyl) and their respective analogs, **1A–3A** (R = 2,6-diisopropylphenyl).*
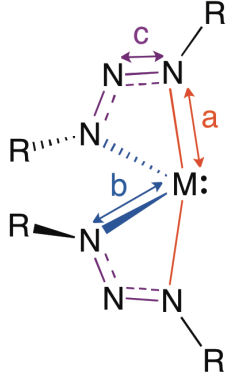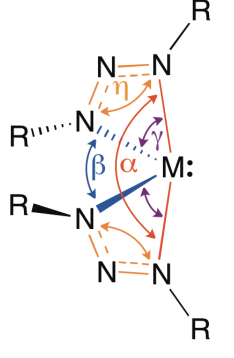
| | | Ge | | Sn | | Pb | |
|---|---|------|------|------|------|------|------|
| | | **1** | **1A** | **2** | **2A** | **3** | **3A** |
| | a | 2.217 | 2.195 | 2.388 | 2.339 | 2.503 | 2.46 |
| | b | 1.995 | 2.008 | 2.207 | 2.223 | 2.326 | 2.35 |
| | c | 1.31 | 1.31 | 1.31 | 1.31 | 1.29 | 1.30 |

*Table 2. Bond angles in degrees (°) for **1–3** (R=tert-butyl) and their respective analogs, **1A–3A** (R = 2,6-diisopropylphenyl).*

| | | Ge | | Sn | | Pb | |
|---|---|------|------|------|------|------|------|
| | | **1** | **1A** | **2** | **2A** | **3** | **3A** |
| | α | 147.9 | 137.37 | 133.39 | 129.18 | 129.61 | 125.5 |
| | β | 98.2 | 104.7 | 93.99 | 101.4 | 92.13 | 100.5 |
| | γ | 59.64 | 59.61 | 54.87 | 55.3 | 52.54 | 52.8 |
| | η | 107.35 | 106.7 | 110.27 | 108.4 | 112.21 | 109.5 |

Geometries of **1–3** obtained from quantum-chemical density functional theory (DFT) computations are in good agreement with their crystal structures (see supporting information). The stereo-chemically active lone pair of **1** resides in the highest occupied molecular orbital (HOMO) (Figure 3).
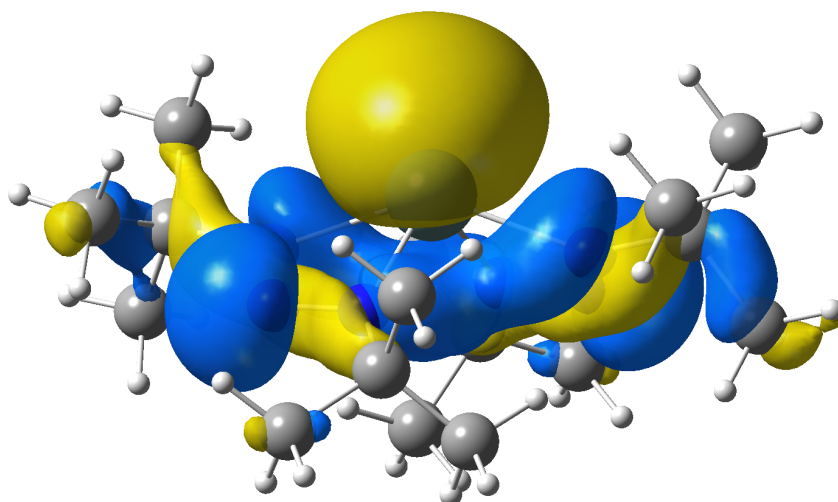
*Figure 3: The HOMO for **1** obtained from DFT calculations. The lone pair reside in the HOMO and occupy a large part of the coordination sphere on the metal center.*

## Thermal properties of Triazenides **1**–**3**

By thermogravimetric analysis (TGA), **1**–**3** volatilize in a single step with onsets between 137–152 °C and negligible residual mass (Figure 4, Table 3). Compound **1** and **3** are therefore the first examples of volatile tetracoordinated M–N bonded Ge(II) and Pb(II) compounds potentially useful for vapor deposition. The mass loss curvse of **1** and **3** (10 mg lass loading) are nearly congruent to curves recorded for their respective cyclic diamides (40 mg lass loading) for TGA data aquired under similar conditions. This qualitative comparison is in agreement with the lower volatility expected for the tetracoordinated compounds compared to their dicoordinated congeners.[24,40] This is also the case for the Sn(II) formamidinate. Compound **2** is only slightly less volatile than Sn(II) formamidinate.[28] This is noteworthy as the formamidinate is the most volatile tetracoordinated M–N bonded Sn(II) literature compound.
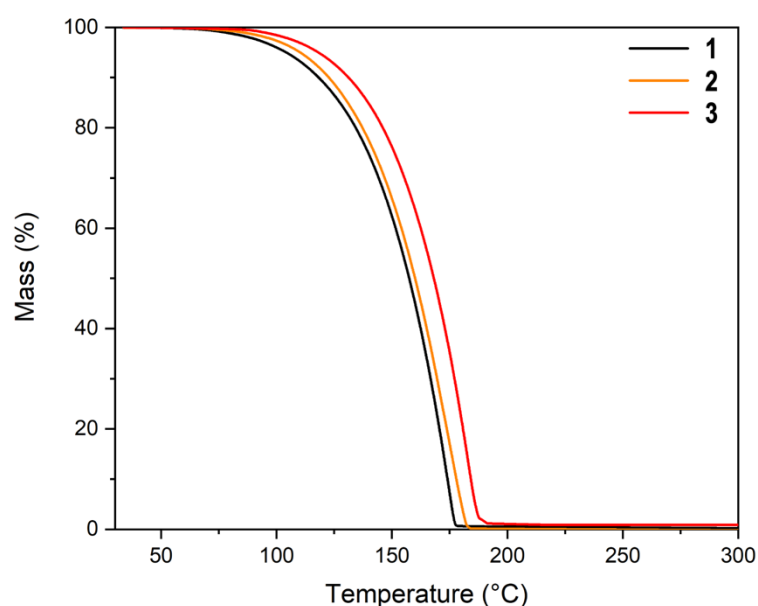


*Figure 4. TGA of compounds **1**–**3** (10 mg samples), showing single step volatilization with negligible residual mass.*

Differential scanning calorimetry (DSC) showed that **1** has an onset of decomposition at 181 °C (see supporting information). The irregular peak shapes indicate overlapping exothermic events. Compound **2** has an onset of decomposition at 175 °C, the main peak is preceded by a shoulder at 160 °C. An additional exothermic event occurs for **2** at ~280 °C. For compound **3**, an exotherm is observed at 85 °C, coinciding with the measured melting point at 83–84 °C. However, no changes occurred when repeatedly heating the compound to 110 °C for hours in a sealed tube other than the compound melting and solidifying. The $^1$H NMR spectrum of the heated compound showed no signs of decomposition, indicating that the exotherm is not a decomposition event. A sharp exotherm, of overlapping signals is observed at 170 °C, similar to that of the main exotherm for **2**. Furthermore, a broad exotherm is observed between 270–300 °C. Results from TGA and DSC are summarized in Table 3 and the figures are displayed in the supporting information.

*Table 3: Summarized TGA and DSC results for **1**–**3**.*

| | 1$^{st}$ DSC exotherm onset (°C) | Onset of volatilization (°C) | Residual mass (%) |
|---|---|---|---|
| **1** | 181 | 137 | 0 |
| **2** | 160 | 140 | 0 |
| **3** | 170* | 152 | 0 |

*The first peak in the DSC is most likely not a decomposition event, indicated by heating the compound in a sealed tube. Therefore, the temperature represents the second exotherm in the DSC.

Disregarding the first exotherm for compound **3**, the onsets of decomposition for **1**–**3** from DSC are well above their onset of volatilization. DSC reveal no thermal events occurring for **1** and **2** below 100 °C, consistent with the observations during melting point measurement. When heating compounds **1** and **2** in sealed tubes, gas bubbles formed in the melts at ~200 and 275 °C, respectively. The melts re-solidified upon cooling as long as the compounds were kept only slightly above the temperature where gas bubbles formed. Increasing the temperature led to bubbles forming at an increased rate and the compounds no longer re-solidified upon cooling. Compound **3** partially decomposed, turning dark at ~180 °C. Upon cooling, the melt re-solidified into an inhomogeneous, yellow and grey solid.

Compounds **1**–**3** sublime between 60–75 °C at 0.5 mbar. However, the compounds partially decompose upon sublimation. Higher yields of compounds **1** and **3** was recovered when performing sublimation at 120–130 °C and atmospheric pressure (~80%) compared to 70–80

°C and reduced pressure (~50%). To account for the observed thermal properties, we studied potential decomposition pathways using DFT computations.

## Computational investigation into the thermal decomposition of 1–3.

DFT was employed to investigate potential decomposition pathways for **1–3**. The pathway with smallest free energy barrier ($\Delta G^{\ddagger}$) for the rate determining step relies on protons migrating between neighboring ligands. In the pathway, one ligand escapes as a free molecule of triazene while the other ligand decomposes into an imido ligand whilst releasing dinitrogen and methylpropene. Figure 5 displays the free-energy profile for compound **2**. Other decomposition pathways may form more than one molecule of dinitrogen, thereby resulting in a significantly lower free energy for the overall decomposition. The presented pathway is most likely kinetically controlled, occurring under relatively mild conditions. See supporting information for optimized geometries and, electronic- and thermal data for all intermediate and transition state structures.
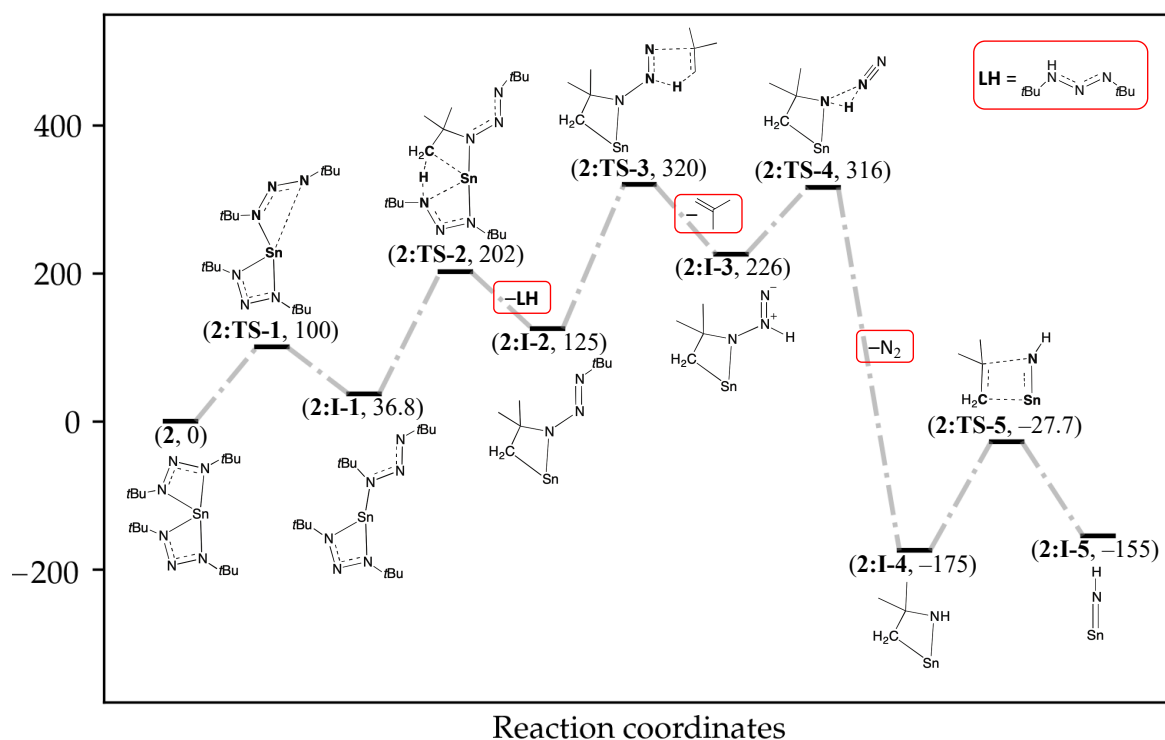


Figure 5: Free energy profile (at 100 °C and 10 hPa) for intermediates and transition states of the inter-ligand decomposition pathway for **2**. The free energy for all geometries are relative to that of **2** and given in kJ mol$^{-1}$. The adduct structure **2:I-2A** is not displayed as separation of **2:I-2** and the triazene ligand is barrierless and have $\Delta G < 0$. Largest free energy barrier is found for **TS-3** (195 kJ mol$^{-1}$). Overall, the decomposition is exergonic due to the release of dinitrogen after **TS-4**.

The decomposition starts with a one ligand de-chelating 180° rotation about a N–N bond in the ligand backbone, transforming **1–3**, via **TS-1**, into **I-1**. The rotation breaks one M–N bond and the ligand de-chelates to adopt a monodentate binding mode. In comparison to the chelating ligand, de-chelation allows the *tert*-butyl on the coordinated nitrogen closer to the metal center and neighboring ligand, which opens up the path for **TS-2**. The transformation of **I-1** into **I-2**

involves the *tert*-butyl group on the coordinated nitrogen, the metal center and the neighboring ligand. During **TS-2**, a proton of the *tert*-butyl group migrates to a coordinated nitrogen on the neighboring ligand. During the migration, the deprotonated ligand chelates as carbon forms a bond to the metal center. Meanwhile, the protonated ligand regains a bidentate binding mode while protonation causes the neighboring ligand to dechelate. Prior to **I-2A**, both ligands are monoanionic. After passing **TS-2,** however, the deprotonated and protonated ligand become dianionic and neutral, respectively. **I-2A** undergo barrierless separation into **I-2** and free 1,3-di-*tert*-butyltriazene (**LH**) (Scheme 2) with $\Delta G < 0$ above –10 and 30 °C at 10 hPa and atmospheric pressure, respectively. Furthermore, if **I-2A** separates under continuous pumping, **LH** may escape **I-2** and be pumped away, preventing recombination of the adduct structure. We therefore assume that **I-2A** separate irreversibly to form **I-2** before decomposing further.
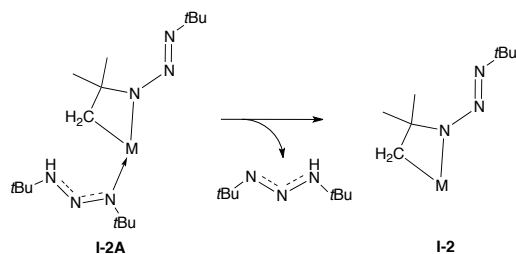


*Scheme 2: Separation of the adduct structure, **I-2A** into **I-2** and free 1,3-di-*tert*-butyltriazene.*

**I-2** decomposes in three irreversible steps, releasing fragments of the dianionic ligand. From **I-2**, a methyl proton of the intact *tert*-butyl group migrates to the α-nitrogen (with respect to the coordinated nitrogen). Passing **TS-3**, the deprotonated *tert*-butyl group leave as methylpropene, resulting in **I-3**. From **I-3**, the proton on the α-nitrogen migrates either to the coordinated nitrogen or to the β-nitrogen. The proton migrating to the coordinated nitrogen has a considerably smaller $\Delta G^{\ddagger}$ compared to the alternative (see supporting information). We therefore follow the path through **TS-4**, where the proton migrates to the coordinated nitrogen. When approaching **I-4**, the α- and β-nitrogens leave as dinitrogen, resulting in a substantial decrease in the free energy. In the last step, when passing **TS-5**, the former *tert*-butyl group (that coordinated to the metal during **TS-2**) is released as methylpropene to give **I-5**: a three-atom complex, consisting of the metal center bearing a linear imido ligand. Calculations show that the singlet state of **I-5** is energetically favored over the triplet state for all three compounds.

Table 4 displays the $\Delta G^{\ddagger}$ for each compound and step in the decomposition pathway. Compared to **1**, compounds **2** and **3** have a significantly larger $\Delta G^{\ddagger}$ for **TS-1**. Compounds **1**–**3** have similar $\Delta G^{\ddagger}$ for **TS-2** to **TS-5**.

*Table 4: Free energy barrier (in kJ mol⁻¹) for each step (in the forward direction) of compounds 1–3 at 100 °C, 10 hPa.*

|       | 1     | 2     | 3     |
|-------|-------|-------|-------|
| **TS-1** | 58.1  | 100   | 111   |
| **TS-2** | 159   | 165   | 169   |
| **TS-3** | 196   | 195   | 193   |
| **TS-4** | 84.4  | 89.9  | 91.8  |
| **TS-5** | 146   | 147   | 147   |

Electron impact mass spectrometry (EI-MS) data of **2** shows signals at *m/z* 176.0 and 134.9 matching [**I-4** – CH$_3$]$^+$ and [**I-5**]$^+$, respectively (see supporting information). Although **I-5** cannot decompose further, this structure is, most likely, highly surface reactive. Furthermore, during vapor deposition, the small size would allow many molecules of **I-5** to adsorb onto the surface without blocking neighboring surface sites resulting in high growth rates.

## Conclusions

In summary we have presented volatile Ge, Sn, and Pb triazenides and shown their potential as precursors for vapor deposition. To our knowledge, **1** and **3** are the first example of tetracoordinated and exclusively M–N bonded Ge and Pb compounds. These compounds show nearly ideal volatilization by TGA with onsets between ~130–160 °C, which are ~20–40 °C below the decomposition observed by DSC. Despite their excellent performance by TGA, the compounds partially decompose during sublimation. Using DFT, a gas-phase decomposition pathway was mapped out which is consistent with EI-MS data. In the decomposition pathway, a neutral ligand is formed that leaves the complex with relative ease. The separation account for the unusual thermal properties of the compounds, where recombination plays an important role in their overall stability. According to the proposed pathway, the group 14 triazenides decompose into a highly surface reactive species containing only the group 14 metal, nitrogen and hydrogen. We believe that, if properly tuned, group 14 triazenide precursors may undergo in situ activation with the potential of yielding superior quality group 14 thin film materials.

## Experimental details

*Caution! As catenated nitrogen compounds are known to be associated with explosive hazards,* tert-*butylazide and compounds **1**–**3** are possible explosive energetic materials. Although we have not experienced any problems in the synthesis, characterization, sublimation, heating and handling of compounds **1**–**3**, their energetic properties have not been fully investigated and are therefore unknown. We therefore highly recommend all appropriate standard safety precautions for handling explosive materials (safety glasses, face shield, blast shield, leather*

*gloves, polymer apron, and ear protection) be used at all times when working with* tert-*butylazide, and compounds **1**–**3***.

All reactions and manipulations were carried out under a $N_2$ atmosphere, either on a Schlenk line using Schlenk air-free techniques, or in a dry box. All anhydrous solvents were purchased from Sigma-Aldrich[TM] and further dried over molecular sieves 4Å. GeCl$_2$•dioxane complex, SnCl$_2$ (98%) and PbCl$_2$ (98%) and *tert*-butyllithium solution (1.7 M in pentane) were purchased from Sigma-Aldrich[TM] and used without further purification. *Tert*-butylazide was prepared according to the literature procedures.[41] All NMR spectra were measured with Oxford Varian 300 and AS500 spectrometers at room temperature unless otherwise stated. Solvent peaks were used as internal standard for the $^1$H NMR (300 and 500 MHz), $^{13}$C NMR (75 and 125 MHz). EI-MS was performed with a Kratos Concept–Magnetic sector Electron impact mass spectrometer in high resolution mode. Melting points were determined in sealed capillaries with a Stuart® SMP10 melting point apparatus and are uncorrected. Elemental analyses were performed by Mikroanalytisches Laboratorium Kolbe, Germany.

## Synthesis of Triazenide Ligand and Compounds **1**–**3**.

### (1,3-di-*tert*-butyltriazenide)lithium(I) Ligand

To a solution of *tert*-butyl azide (18.6 g, 188 mmol) in *n*-hexanes (150 mL) at –78 °C was added dropwise *tert*-butyllithium (1.7 M in pentane, 110 ml, 187 mmol). The reaction mixture was stirred for 30 min and then allowed to warm up to room temperature for 1 h. The reaction mixture was concentrated under reduced pressure to give a light-yellow solid (29.7 g, 97%). This solid was used in the subsequent reactions without further purification. A small amount was purified for characterization by recrystallization from *n*-hexanes at –35 °C to give a solid. Colorless crystals, mp 247–250 °C. $^1$H NMR (300 MHz, C$_6$D$_6$) $\delta$ 1.28 (s, C*H$_3$*, 18H). $^{13}$C{$^1$H} NMR (75 MHz, C$_6$D$_6$) $\delta$ 30.7 (s, C*H$_3$*), 56.7 (s, $C_q$). Anal. calcd for C$_8$H$_{18}$LiN$_3$: C, 58.88%; H, 11.12%; N, 25.75%. Found: C, 58.88%; H, 11.14%; N, 25.67%.

### Bis(1,3-di-*tert*-butyltriazenide)germanium(II) (1)

A solution of (1,3-di-*tert*-butyltriazenide)lithium(I) (3.83 g, 23.5 mmol) in THF (20 mL) at –35 °C was added dropwise to a solution of GeCl$_2$•dioxane (2.73 g, 11.7 mmol) in THF (30 mL) at –35 °C. The whole was held at –35 °C for 10 min and then stirred at room temperature for 16 h. The reaction mixture was concentrated under reduced pressure and the resulting residue was suspended in *n*-hexane, filtered through a pad of Celite® and concentrated under reduced

pressure to give the crude product. The crude was purified by recrystallization from THF/MeCN at –35 °C to give **1** as a solid (3.39 g, 75%).

**1**: Pale yellow solid, mp 82–84 °C. Sublimation: ~60 °C (0.5 mbar). $^1$H NMR (300MHz, $C_6D_6$) $\delta$ 1.40 (s, 36H, C$H_3$). $^{13}$C{$^1$H} NMR (125 MHz, $C_6D_6$) $\delta$ 30.6 (s, $CH_3$), 59.1 (s, $C_q$). EI-MS (LR): 230.1 (100%), 245.1 (<5%), 287.1 (<5%), 329.2 (25%), 386.2 (30%). Anal. calcd for $C_{16}H_{36}GeN_6$: C, 49.90%; H, 9.42%; N, 21.82%. Found: C, 49.70%; H, 9.40%; N, 21.78%.

**Bis(1,3-di-*tert*-butyltriazenide)tin(II) (2)**

A solution of (1,3-di-*tert*-butyltriazenide)lithium(I) (1.25 g, 7.65 mmol) in a 1:4 mixture of $Et_2O$/*n*-hexane (5 mL) at –35 °C was added dropwise to a suspension of $SnCl_2$ (0.17 g, 0.91 mmol) in *n*-hexane (5 mL) at –35 °C and then stirred at room temperature for 16 h. The reaction mixture was filtered through a pad of Celite® and concentrated under reduced pressure to give the crude product. The crude was purified by recrystallization from THF/MeCN at –35 °C to give **2** as a solid (0.79 g, 88%).

**2**: Yellow solid, mp 58–59 °C. Sublimation: ~65 °C (0.5 mbar). $^1$H NMR (500 MHz, $C_6D_6$) $\delta$ 1.35 (s, 36H, C$H_3$). $^{13}$C{$^1$H} NMR (125 MHz, $C_6D_6$) $\delta$ 30.6 (s, $CH_3$), 58.9 (s, $C_q$). EI-MS (LR): 134.9 (8%), 274.1 (8%), 373.1 (<5%), 432.2 (25%). Anal. calcd for $C_{16}H_{36}N_6Sn$: C, 44.57%; H, 8.41%; N, 19.49%. Found: C, 44.04%; H, 8.31%; N, 19.23%.

**Bis(1,3-di-*tert*-butyltriazenide)lead(II) (3)**

Compound **3** was synthesized in the same manner as **2** using a solution of (1,3-di-*tert*-butyltriazenide)lithium(I) (1.43 g, 8.76 mmol) in a 1:4 mixture of $Et_2O$/*n*-hexane (20 mL), and a suspension of $PbCl_2$ (1.22 g, 4.39 mmol) in *n*-hexane (20 mL). The crude was purified by recrystallization in the same manner of compound **2** to give **3** as a solid (1.58 g, 69%).

**3**: Yellow solid, mp 83–84 °C. Sublimation: ~75 °C (0.5 mbar). $^1$H NMR (500 MHz, $C_6D_6$) $\delta$ 1.30 (s, 36H, C$H_3$). $^{13}$C{$^1$H} NMR (125 MHz, $C_6D_6$) $\delta$ 30.5 (s, $CH_3$), 61.1 (s, $C$). Anal. calcd for $C_{16}H_{36}N_6Pb$: C, 36.98 %; H, 6.98%; N, 16.17%. Found: C, 36.56%; H, 6.97%; N, 16.03%.

## Structure determination by single crystal x-ray diffraction

Single crystals for **1**–**3** were obtained by recrystallization from THF/MeCN at –35 °C. The single crystals were used for X-ray diffraction data collection on a Bruker D8 SMART Apex-II diffractometer, using graphite-monochromated Mo–Kα radiation ($\lambda$ = 0.71073 Å) at 153 K. All data were collected in hemisphere with over 95% completeness to $2\theta < 50.05°$. The structures were solved by direct methods. Coordinates of metal atoms were determined from

the initial solutions, and of the N and C methods were located in subsequent differential Fourier syntheses. The solution does not contain much of residual electron density, but it stays for multitude of additional possible positions of light atoms. All non-hydrogen atoms were refined, first in isotropic and then in anisotropic approximation, using Bruker SHELXTL software. Selected crystal data are summarized below. The hydrogen atoms were added in riding approximation and refined isotropically.

**1**: $C_{16}H_{36}GeN_6$, M = 385.12, Monoclinic, space group P2/c, a = 9.702(7), b = 6.055(5), c = 18.549(14) Å, $\alpha$ = 90, $\beta$ = 100.971(9), $\gamma$ = 90°, V = 1069.6(14) Å$^3$, Z = 2, $D_c$ = 1.196 g/cm$^{-3}$, $\mu$ = 1.440 mm$^{-1}$, T = 153 K, 6500 reflections measured, 1877 unique, final $R1$ [$I > 2\sigma(l)$] = 0.0254, wR2 (all data) = 0.0672, GOF = 1.040.

**2**: $C_{16}H_{36}N_6Sn$, M = 431.20, Orthorhombic, space group Pbcn, a = 12.732(5), b = 13.049(5), c = 13.693(6) Å, V = 2274.9(16) Å$^3$, Z = 4, $D_c$ = 1.259 g/cm$^{-3}$, $\mu$ = 1.131 mm$^{-1}$, T = 153 K, 16479 reflections measured, 2051 unique, final $R1$ [$I > 2\sigma(l)$] = 0.0256, wR2 (all data) = 0.0696, GOF = 0.934.

**3**: $C_{16}H_{36}N_6Pb$, M = 519.70, Orthorhombic, space group Pbcn, a = 12.786(4), b = 12. 794(4), c = 13.734(4) Å. V = 2246.7(12) Å$^3$, Z = 4, $D_c$ = 1.536 g/cm$^3$, $\mu$ = 7.518 mm$^{-1}$, T = 153 K, 15085 reflections measured, 1982 unique, final $R1$ [$I > 2\sigma(l)$] = 0.0236, wR2 (all data) = 0.0795, GOF = 0.936.

CCDC 2058914 for **1,** 2058915 for **2**, and 2058916 for **3** contain supplementary crystallographic data for this paper. These data can be obtained free of charge from the Cambridge Crystallographic Data Centre.

## Thermogravimetric analysis

TGA was performed on Pt pans with a TA Instruments Q50 housed in an MBraun Labmaster 130 dry box filled with nitrogen gas (99.998 % purity). Pt pans were cleaned by ultrasonication, first in dilute nitric acid (~3 N), then water, and lastly 2-propanol. The pans were heated until red hot in air by a propane torch, remove any remaining impurities. During the TGA experiments of **3**, if the compound decomposes then Pb(0) might form and, consequently, alloy with the Pt pans. To avoid potential alloying, pans used for TGA of **3** were coated with a 55 nm $Al_2O_3$ layer as a precaution. The coating was grown at 200 °C, using TMA and water—0.1 s pulses and 8 s purges each—for 500 cycles.[31] All TGA experiments were performed under a

flow of ultrapure nitrogen (99.999%, 60 sccm). For ramp experiments, samples were heated to 500 °C at a rate of 10 °C min$^{-1}$. Isothermal TGA were carried out at 90 °C and 110 °C. To rapidly reach the desired temperature, a heating rate of 40 °C min$^{-1}$ was used. The experiments were carried out with the same mass loadings as ramp experiments. Onset of volatilization was defined as the intersect between tangent lines of the plateau and the slope.

## Differential scanning calorimetry

DSC experiments were performed using a TA Instruments Q10 instrument. Inside a glovebox, samples of $(0.30 \pm 0.03)$ mg of **1**–**3** were sealed in aluminum pans. Unless otherwise stated, all samples were heated to 400 ºC at a rate of 10 ºC min$^{-1}$. Dinitrogen (99.998%) was used as purge gas. Experiments were performed in triplicate with similar mass loadings to ensure the validity of the recorded data. Onset of decomposition was defined as a 5% increase in exothermic heat flow from the beginning of the exothermic event.

## Density functional theory

All quantum chemical computations were preformed using Gaussian 16 software.[42] Structural optimization and harmonic normal mode vibrational calculations were done using the hybrid DFT method B3LYP[43,44] together with Grimme's version 3 dispersion correction[45] and def2TZVP[46,47] basis set. Decomposition pathways were investigated by searching for possible stable structures as well as finding transition states. Transition states were connected to neighboring intermediate structures by following the transition state's intrinsic reaction coordinate. Minima were confirmed having no imaginary frequencies, while transition states were verified to have one imaginary frequency, lying along the reaction path.

## References

(1)     Anne, M.-L.; Keirsse, J.; Nazabal, V.; Hyodo, K.; Inoue, S.; Boussad-Pledel, C.; Lhermite, H.; Charrier, J.; Yanakata, K.; Loreal, O.; Le Person, J.; Colas, F.; Compère, C.; Bureau, B. Chalcogenide Glass Optical Waveguides for Infrared Biosensing. *Sensors* **2009**, *9*, 7398–7411.

(2)     Antunez, P. D.; Buckley, J. J.; Brutchey, R. L. Tin and Germanium Monochalcogenide IV–VI Semiconductor Nanocrystals for Use in Solar Cells. *Nanoscale* **2011**, *3*, 2399–2411.

(3)     Sinsermsuksakul, P.; Hartman, K.; Kim, S. B.; Heo, J.; Sun, L.; Park, H. H.; Chakraborty, R.; Buonassisi, T.; Gordon, R. G. Enhancing the Efficiency of SnS Solar Cells via Band-Offset Engineering with a Zinc Oxysulfide Buffer Layer. *Appl. Phys. Lett.* **2013**, *102*, 053901.

(4)     Sun, L.; Haight, R.; Sinsermsuksakul, P.; Kim, S. B.; Park, H. H.; Gordon, R. G. Band Alignment of SnS/Zn(O,S) Heterojunctions in SnS Thin Film Solar Cells. *Appl. Phys. Lett.* **2013**, *103*, 181904.

(5)     Greyson, E. C.; Barton, J. E.; Odom, T. W. Tetrahedral Zinc Blende Tin Sulfide Nano- and Microcrystals. *Small* **2006**, *2*, 368–371.

(6)     Jiang, T.; Ozin, G. A. New Directions in Tin Sulfide Materials Chemistry. *J. Mater. Chem.* **1998**, *8*, 1099–1108.

(7)     Alexandros, S.; Jason, M. S.; Christopher, A. C.; Andrew, G. C.; Patrick, S. G.; Andrew, A. R. W. SnS/PbS Nanocrystal Heterojunction Photovoltaics. *Nanotechnology* **2010**, *21*, 185202.

(8)     Sinsermsuksakul, P.; Chakraborty, R.; Kim, S. B.; Heald, S. M.; Buonassisi, T.; Gordon, R. G. Antimony-Doped Tin(II) Sulfide Thin Films. *Chem. Mater.* **2012**, *24*, 4556–4562.

(9)     Kim, J. Y.; George, S. M. Tin Monosulfide Thin Films Grown by Atomic Layer Deposition Using Tin 2,4-Pentanedionate and Hydrogen Sulfide. *J. Phys. Chem. C* **2010**, *114*, 17597–17603.

(10)    Bernades-Silva, A. C.; Mesquita, A. F.; de Moura Neto, E.; Porto, A. O.; de Lima, G. M.; Ardisson, J. D.; Lameiras, F. S. Tin Selenide Synthesized by a Chemical Route: The Effect of Theannealing Conditions in the Obtained Phase. *Solid State* **2005**, *135*, 677–682.

(11)    Liu, S.; Guo, X.; Li, M.; Zhang, W.-H.; Liu, X.; Li, C. Solution-Phase Synthesis and Characterization of Single-Crystalline SnSe Nanowires. *Angew. Chem. Int. Ed.* **2011**,

*50*, 12050–12053.

(12)   Mathews, N. R. Electrodeposited Tin Selenide Thin Films for Photovoltaic Applications. *Sol. Energy* **2012**, *86*, 1010–1016.

(13)   Moon, D. G.; Rehan, S.; Yeon, D. H.; Lee, S. M.; Park, S. J.; Ahn, S. J.; Cho, Y. S. A Review on Binary Metal Sulfide Heterojunction Solar Cells. *Sol. Energy Mater. Sol. Cells* **2019**, *200*, 109963.

(14)   Yeon, D. H.; Mohanty, B. C.; Lee, C. Y.; Lee, S. M.; Cho, Y. S. High-Efficiency Double Absorber PbS/CdS Heterojunction Solar Cells by Enhanced Charge Collection Using a ZnO Nanorod Array. *ACS Omega* **2017**, *2*, 4894–4899.

(15)   Safrani, T.; Kumar, T. A.; Klebanov, M.; Arad-Vosk, N.; Beach, R.; Sa'Ar, A.; Abdullhalim, L.; Sarusi, G.; Golan, Y. High-Efficiency Double Absorber PbS/CdS Heterojunction Solar Cells by Enhanced Charge Collection Using a ZnO Nanorod Array. *J. Mater. Chem. C* **2014**, *2*, 9132–9140.

(16)   Lee, S. M.; Jang, W.; Mohanty, B. C.; Yoo, J.; Jang, J. W.; Kim, D. B.; Yi, Y.; Soon, A.; Cho, Y. S. Experimental Demonstration of in Situ Stress-Driven Optical Modulations in Flexible Semiconducting Thin Films with Enhanced Photodetecting Capability. *Chem. Mater.* **2018**, *30*, 7776–7781.

(17)   Carrillo-Castillo, A.; Salas-Villasenor, A.; Mejia, I.; Aguirre-Tostado, S.; Gnade, B. E.; Quevedo-López, M. A. P-Type Thin Films Transistors with Solution-Deposited Lead Sulfide Films as Semiconductor. *Thin Solid Films* **2012**, *520*, 3107–3110.

(18)   Navale, S. T.; Bandgar, D. K.; Chougule, M. A.; Patil, V. B. Facile Method of Preparation of PbS Films for NO2 Detection. *RSC Adv.* **2015**, *5*, 6518–6527.

(19)   Beatriceveena, T. V.; Prabhu, E.; Murthy Sree Rama, A.; Jayaraman, V.; Gnanasekar, K. I. Highly Selective PbS Thin Film Based Ammonia Sensor for Inert Ambient: In-Situ Hall and Photoelectron Studies. *Appl. Surf. Sci.* **2018**, *456*, 430–436.

(20)   Hatanpää, T.; Ritala, M.; Leskelä, M. Precursors as Enablers of ALD Technology: Contributions from University of Helsinki. *Coord. Chem. Rev.* **2013**, *257*, 3297–3322.

(21)   Koponen, S. E.; Gordon, P. G.; Barry, S. T. Principles of Precursor Design for Vapour Deposition Methods. *Polyhedron* **2016**, *108*, 59–66.

(22)   George, S. M. Atomic Layer Deposition: An Overview. *Chem. Rev.* **2010**, *110*, 111–131.

(23)   Gordon, R. G. Atomic Layer Deposition for Semiconductors. In *Atomic Layer Deposition for Semiconductors*; Hwang, C. S., Yoo, C. Y., Eds.; Springer US: New York, 2014; pp 15–46.

(24) Kim, S. B.; Sinsermsuksakul, P.; Hock, A. S.; Pike, R. D.; Gordon, R. G. Synthesis of N-Heterocyclic Stannylene (Sn(II)) and Germylene (Ge(II)) and a Sn(II) Amidinate and Their Application as Precursors for Atomic Layer Deposition. *Chem. Mater.* **2014**, *26*, 3065–3073.

(25) Gynane, M. J. S.; Harris, D. H.; Lappert, M. F.; Power, P. P.; Rivière, P.; Rivière-Baudet, M. Subvalent Group 4B Metal Alkyls and Amides. Part 5. The Synthesis and Physical Properties of Thermally Stable Amides of Germanium(II), Tin(II), and Lead(II). *J. Chem. Soc., Dalton Trans.* **1977**, 2004–2009.

(26) Yoo, C.; Kim, W.; Jeon, J. W.; Park, E. S.; Ha, M.; Lee, Y. K.; Hwang, C. S. Atomic Layer Deposition of Ge XSe1- x Thin Films for Endurable Ovonic Threshold Selectors with a Low Threshold Voltage. *ACS Appl. Mater. Interfaces* **2020**, *12*, 23110–23118.

(27) Sinsermsuksakul, P.; Heo, J.; Noh, W.; Hock, A. S.; Gordon, R. G. Atomic Layer Deposition of Tin Monosulfide Thin Films. *Adv. Energy Mater.* **2011**, *1*, 1116–1125.

(28) Kim, S. B.; Zhao, X.; Davis, L. M.; Jayaraman, A.; Yang, C.; Gordon, R. G. Atomic Layer Deposition of Tin Monosulfide Using Vapor from Liquid Bis(N, N′-Diisopropylformamidinato)Tin(II) and H2S. *ACS Appl. Mater. Interfaces* **2019**, *11*, 45892–45902.

(29) Popov, G.; Bačić, G.; Mattinen, M.; Manner, T.; Lindström, H.; Seppänen, H.; Suihkonen, S.; Vehkamäki, M.; Kemell, M.; Jalkanen, P.; Mizohata, K.; Räisänen, J.; Leskelä, M.; Koivula, H. M.; Barry, S. T.; Ritala, M. Atomic Layer Deposition of PbS Thin Films at Low Temperatures. *Chem. Mater.* **2020**, *32*, 8216–8228.

(30) Popov, G.; Mattinen, M.; Hatanpää, T.; Vahkamäki, M.; Kemell, M.; Mizohata, K.; Räisänen, J.; Ritala, M.; Leskelä, M. Atomic Layer Deposition of PbI2 Thin Films. *Chem. Mater.* **2019**, *31*, 1101–1109.

(31) Bačić, G.; Zanders, D.; Mallick, B.; Devi, A.; Barry, S. T. Designing Stability into Thermally Reactive Plumbylenes. *Inorg. Chem.* **2018**, *57*, 8218–8226.

(32) Karsch, H. H.; Schlüter, P. A.; Reisky, M. Bis(Amidinate) Complexes of Silicon and Germanium. *Eur. J. Inorg. Chem.* **1998**, No. 4, 433–436.

(33) Chlupatý, T.; Padělková, Z.; Lyčka, A.; Brus, J. Reactivity of Lithium N-Butyl Amidinates towards Group 14 Metal(II) Chlorides Providing Series of Hetero- and Homoleptic Tetrylenes. *Dalton Trans.* **2012**, *41*, 5010–5019.

(34) Flanagan, K. R.; Parish, J. D.; Fox, M. A.; Johnson, A. L. Synthetic, Structural, and Computational Studies on Heavier Tetragen and Chalcogen Triazenide Complexes. *Inorg. Chem.* **2019**, *58*, 16660–16666.

(35)  O'Brien, N. J.; Rouf, P.; Samii, R.; Rönnby, K.; Buttera, S. C.; Hsu, C.-W.; Ivanov, I. G.; Kessler, V.; Ojamäe, L.; Pedersen, H. In-Situ Activation of an Indium(III) Triazenide Precursor for Epitaxial Indium Nitride by Atomic Layer Deposition. *Chem. Mater.* **2020**, *32*, 4481–4489.

(36)  Rouf, P.; Samii, R.; Rönnby, K.; Bakhit, B.; Buttera, S. C.; Martinovic, I.; Ojamäe, L.; Hsu, C.-W.; Kessler, V.; Palisaitis, J.; Kessler, V.; Pedersen, H.; O'Brien, N. J. Hexacoordinated Gallium(III) Triazenide Precursor for Epitaxial Gallium Nitride by Atomic Layer Deposition. *ChemRxiv* **2020**, https://doi.org/10.26434/chemrxiv.13190636.v1.

(37)  Samii, R.; Zanders, D.; Buttera, S. C.; Kessler, V.; Ojamäe, L.; Pedersen, H.; O'Brien, N. J. Synthesis and Thermal Study of Hexacoordinated Aluminum(III) Triazenides for Use in Atomic Layer Deposition. *Inorg. Chem.* **2021**, *in press*. https://doi.org/10.1021/acs.inorgchem.0c03496.

(38)  Rosiak, D.; Okuniewski, A.; Chojnacki, J. Novel Complexes Possessing Hg–(Cl, Br, I)···O=C Halogen Bonding and Unusual Hg2S2(Br/I)4 Kernel. The Usefulness of T4′ Structural Parameter. *Polyhedron* **2018**, *146*, 35–41.

(39)  Bent, H. A. An Appraisal of Valence-Bond Structures and Hybridization in Compounds of the First-Row Elements. *Chem. Rev.* **1961**, *61*, 275–311.

(40)  Bačić, G.; Zanders, D.; Mallick, B.; Devi, A.; Barry, S. T. Designing Stability into Thermally Reactive Plumbylenes. *Inorg. Chem.* **2018**, *57*, 8218–8226.

(41)  Bottaro, J. C.; Penwell, P. E.; Schmitt, R. J. Expedient Synthesis of T-Butyl Azide. *Synth. Commun.* **1997**, *27*, 1465–1467.

(42)  Frisch, M. J.; Trucks, G. W.; Schlegel, H. B.; Scuseria, G. E.; Robb, M. A.; Cheeseman, J. R.; Scalmani, G.; Barone, V.; Petersson, G. A.; Nakatsuji, H.; Li, X.; Caricato, M.; Marenich, A. V.; Bloino, J.; Janesko, B. G.; Gomperts, R.; Mennucci, B.; Hratchian, H. P.; Ortiz, J. V.; Izmaylov, A. F.; Sonnenberg, J. L.; Williams-Young, D.; Ding, F.; Lipparini, F.; Egidi, F.; Goings, J.; Peng, B.; Petrone, A.; Henderson, T.; Ranasinghe, D.; Zakrzewski, V. G.; Gao, J.; Rega, N.; Zheng, G.; Liang, W.; Hada, M.; Ehara, M.; Toyota, K.; Fukuda, R.; Hasegawa, J.; Ishida, M.; Nakajima, T.; Honda, Y.; Kitao, O.; Nakai, H.; Vreven, T.; Throssell, K.; Montgomery, J. A., J.; Peralta, J. E.; Ogliaro, F.; Bearpark, M. J.; Heyd, J. J.; Brothers, E. N.; Kudin, K. N.; Staroverov, V. N.; Keith, T. A.; Kobayashi, R.; Normand, J.; Raghavachari, K.; Rendell, A. P.; Burant, J. C.; Iyengar, S. S.; Tomasi, J.; Cossi, M.; Millam, J. M.; Klene, M.; Adamo, C.; Cammi, R.; Ochterski, J. W.; Martin, R. L.; Morokuma, K.; Farkas, O.; Foresman,

J. B.; Fox, D. J. Gaussian 16 Revision B.01. 2016.

(43) Hanson-Heine, M. W. D.; George, M. W.; Besley, N. A. Calculating Excited State Properties Using Kohn-Sham Density Functional Theory. *J. Chem. Phys.* **2013**, *138*, 064101.

(44) Lecklider, T. Maintainng a Heathy Rhythm. *EE Eval. Eng.* **2011**, *50*, 36–39.

(45) Grimme, S.; Antony, J.; Ehrlich, S.; Krieg, H. A Consistent and Accurate Ab Initio Parametrization of Density Functional Dispersion Correction (DFT-D) for the 94 Elements H-Pu. *J. Chem. Phys.* **2010**, *132*, 154104.

(46) Weigend, F.; Ahlrichs, R. Balanced Basis Sets of Split Valence, Triple Zeta Valence and Quadruple Zeta Valence Quality for H to Rn: Design and Assessment of Accuracy. *Phys. Chem. Chem. Phys.* **2005**, *7*, 3297–3305.

(47) Bernhard, M.; Stoll, H.; Dolg, M. Small-Core Multiconfiguration-Dirac–Hartree–Fock-Adjusted Pseudopotentials for Post-d Main Group Elements: Application to PhB and PbO. *J. Chem. Phys.* **2000**, *113*, 2563–2569.